Improving global barotropic tides with sub-grid scale topography

He Wang[1,2,3], **Robert W. Hallberg**[2], **Alan J. Wallcraft**[4], **Brian K. Arbic**[3], **and Eric P. Chassignet**[4]

[1]University Corporation for Atmospheric Research, Boulder, CO, USA

[2]Geophyical Fluid Dynamics Laboratory, National Oceanic and Atmospheric Administration, Princeton, NJ, USA

[3]Department of Earth and Environmental Sciences, University of Michigan, Ann Arbor, MI, USA

[4]Florida State University, Tallahassee, FL, USA

Key Points:

- The accuracy of tides in ocean models is affected by the representation of topography, which is constrained by model horizontal resolution.
- The geometric effect of the sub-grid scale topographic features can be approximated in the model with the porous barriers.
- The porous barriers can significantly reduce globally averaged errors for the M_2 barotropic tides.

Corresponding author: He Wang, `he.wang@noaa.gov`

Abstract

In recent years, efforts have been made to include tides in both operational ocean models as well as climate and earth system models. The accuracy of the barotropic tides is often limited by the model topography, which is in turn limited by model horizontal resolution. In this work, we explore the reduction of barotropic tidal errors in an ocean general circulation model (Modular Ocean Model version 6; MOM6) using sub-grid scale topography representation. We follow the methodology from Adcroft (2013), which utilizes statistics from finer resolution topographic datasets to represent sub-grid scale features with a light computational cost in a structured finite volume formulation. The geometric effect from sub-grid scale topography can be introduced to the model with only a few parameters at each grid cell. The porous barriers, which are implemented at the walls of the grid cells, are used to modify transport between grid cells. Our results show that the globally averaged tidal error in lower-resolution simulations is significantly reduced with the use of porous barriers. We argue this is a potentially useful tool to improve simulations of tides (and other flows) in low-resolution simulations.

Plain Language Summary

Tides play a crucial role in predicting future sea level changes. In recent years, significant attention has been given to simulating tides in diverse ocean and climate models, making it essential to enhance the accuracy of these modeled tides. One notable source of tidal errors stems from the representation of ocean floor topography in numerical ocean models, which relies on a fixed number of grid boxes (i.e. model's resolution). Computational limitations often impose constraints on the model's horizontal resolution. Our objective in this study is to enhance the portrayal of ocean topography at a given resolution to minimize tidal errors. To achieve this, we employ a technique known as "porous barriers", which effectively approximates the effects of ocean topography that are omitted in the models, without imposing significant computational burdens. Our findings demonstrate that the incorporation of porous barriers results in a substantial reduction of tidal errors in our ocean model. These results underscore the advantages of utilizing porous barriers not only in tidal simulations but also in numerous other physical processes within the ocean.

1 Introduction

Tides are one of the most prominent phenomena in the ocean. Tides arise from differences in the lunar and solar gravitational potential across the Earth. The astronomical tidal forcing drives periodic changes in sea surface height (SSH) and periodic tidal currents. There is a growing need for better understanding tidal interactions with other physical and biogeochemical processes in a changing climate with shorelines altered by sea-level rise and coastal development.

With the advancement of computational powers, tides have begun to be explicitly included in both operational global ocean models (high horizontal resolution and short time duration) and global climate and earth system models (often run at low horizontal resolution and long time duration) (Thomas et al., 2001; Schiller & Fiedler, 2007; Müller et al., 2010; Arbic et al., 2010; Barton et al., 2022; Arbic, 2022; Pal et al., 2023). For both high- and low-resolution simulations, it is helpful and sometimes even critical to improve the accuracy of the modeled tides. One important source of tidal error arises from the representation of topography.

In the real ocean, tides are affected by ocean topography[1] in many ways. About 1/3 of the global tidal dissipation is carried out by the breaking of internal tides in open-ocean regions with rough topography (Egbert & Ray, 2001). In addition to these small scale dissipative processes that often require parameterizations in models, the resonances of global tides are also sensitive to ocean topography. In open oceans, the semi-closed basins guide the propagations of the shallow-water surface gravity waves (Kelvin Waves and Poincaré Waves) forming the amphidromic points and cotidal lines. In the coastal regions, shoreline configuration, shapes of the marginal seas and connectivity of the channels can all influence local tides. The tides of the open ocean are thought to be weakly resonant (Wunsch, 1972; Heath, 1981) due to the fact that there are many global ocean normal modes with frequencies close to those of the astronomical semidiurnal and diurnal tidal forcing (Platzman et al., 1981; Müller, 2007). Some coastal regions (e.g., the Bay of Fundy, English Channel, Hudson Strait, and other locations) are well-shaped for further resonance (Garrett, 1972; Clarke, 1991; Cummins et al., 2010). Previous work

---

[1] As an abbreviation, we use the term "topography" to refer to ocean basin geometry, ocean bathymetry and shoreline configurations hereinafter.

76   has shown that strongly resonant tides in coastal regions have a "back-effect" on tides

77   in the open ocean (Arbic et al., 2007, 2009; Arbic & Garrett, 2010).

78   Therefore, in order to better simulate tidal resonances in both open oceans, marginal

79   seas and interactions between them, it is crucial to faithfully represent ocean topogra-

80   phy in numerical models. However, the accuracy of ocean topography in models is highly

81   restricted by their horizontal resolutions. For discretized model grids, the degrees of free-

82   dom of ocean topography is inherently limited by the number of grid cells. This restric-

83   tion hinders further reduction of tidal errors at a given resolution. Numerical models are

84   unable to resolve sub-grid scale topographic features such as deep ocean channels, ridges

85   and details of shoreline configurations, which leads to misrepresentations of ocean basin/shoreline

86   geometry and resonances of tides and contributes to higher tidal errors in lower resolu-

87   tion simulations (e.g. Egbert et al., 2004). While parameterizations can be used to par-

88   tially characterize unresolved physical processes such as the energy cascade from barotropic

89   tides to internal tides, the missing geometrical effects due to unresolved topographic fea-

90   tures and basin/shoreline geometry are often unaccounted for. One potential method for

91   improving the quality of the topography and shoreline geometry in the model is to rep-

92   resent the effect of sub-grid scale topography via porous barriers.

93   In this work, we evaluate the effect of porous barriers, on tides, following the method-

94   ology from Adcroft (2013). In essence, porous barriers introduce sub-grid scale topographic

95   information at grid cell walls in finite volume ocean models, which can potentially mit-

96   igate the limitation on topography details imposed by model's horizontal resolution. Tra-

97   ditionally, the grid cell walls in finite volume ocean models are fully-opened and uniformly-

98   wide, and the complicated topography features that grid cell walls transect (as depicted

99   in the left panel of Figure 1) is therefore ignored. The concept of porous barriers is to

100   model the grid cell walls as permeable barriers in which the openness changes vertically.

101   In practice, we use the statistics of the complicated sub-grid depth profile (D_{shallow}, D_{mean}

102   and D_{deep} in Figure 1) and approximate with a simplified structure that widens mono-

103   tonically from the very bottom to the highest point of the topography (e.g. right panel

104   of Figure 1). Effectively, the depth profile acts as a constraint on the actual widths as

105   a function of depth and each model layer is provided with a connectivity across the cell
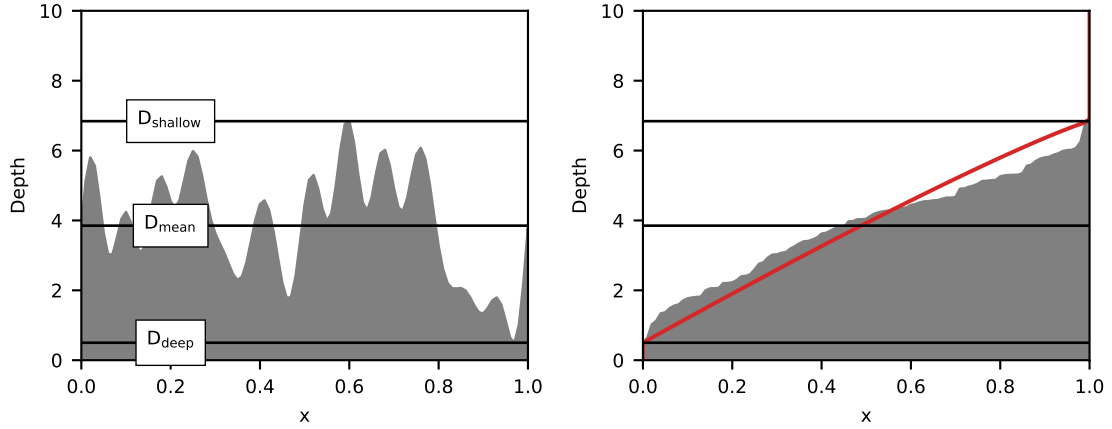
106   walls that matches the real ocean.

Figure 1. Illustration of the concept of a porous barrier at the facet of a single grid cell. Units of both coordinates in this illustration are arbitrary. At each depth, connectivity, measured by the area of openness, is the same for the realistic sub-grid scale topography in the left panel and the sorted topography in the right panel. The sub-grid scale openness (as a function of depth) is used by the model to constrain transports across grid cells. We can further simplify by using parameters likes the maximum, minimum and mean depths to generate an idealized depth profile (red line in the right panel), so that the openness can be solved analytically by the model. The simplified depth profiles are generated following the algorithms in the Appendix of Adcroft (2013).

107 With porous barriers, the model has additional degrees of freedom to represent the

108 topography without increasing the model's horizontal resolution and the computational

109 burden that comes with the increased resolution. In Adcroft (2013), an application to

110 a tsunami event showed that the porous barriers can reduce the error of travel times of

111 the surface gravity wave in low resolution simulations. Here we expand the use of porous

112 barriers to a global implementation and study its application to barotropic tides.

113 We conduct numerical experiments using Modular Ocean Model version 6 (MOM6;

114 Adcroft et al., 2019) as a barotropic tide model. To better simulate tides, we introduce

115 a new inline self-attraction and loading (SAL) scheme in MOM6. The SAL term accounts

116 for the deformation of the seafloor by the load of the seawater, the gravitational self-attraction

117 of the so-deformed solid earth, and the self-attraction of the seawater itself (Hendershott,

118 1972; Ray, 1998). The SAL effect applies to all motions of seawater that change mass

119 (bottom pressure) but is especially important for high-frequency motions such as tides.

120 For tides, the SAL term is approximately equal to 10% of the tidal SSH signal. The cal-

121 culation of SAL requires spherical harmonic transforms of global bottom pressure anomaly,

122 which was historically considered too expensive to calculate inline. Other SAL schemes

123 (e.g., scalar approximation, reading in observed SAL fields, and iterative method) have

124 been adopted to circumvent the need for a fully inline SAL calculation, but these approaches

125 are either highly inaccurate or not applicable to non-tidal motions or evolving tides in

126 a changing climate. In recent years, a number of ocean models and earth system ocean

127 component models have begun to compute SAL inline (Vinogradova et al., 2015; Schin-

128 delegger et al., 2018; Shihora et al., 2022; Barton et al., 2022; Brus et al., 2023). A sim-

129 ilar effort is made in MOM6 and results in this work demonstrate the utility of inline

130 SAL.

131 The key conclusion from this work is that porous barriers significantly improve M_2

132 barotropic tides. We first use a numerical experiment with 0.04° horizontal resolution

133 as a baseline to evaluate tidal simulation in MOM6. Two sets of numerical experiments

134 with various resolutions, with and without porous barriers, are constructed from the base-

135 line experiment. We found globally implemented porous barriers help reduce the increased

136 tidal errors caused by the coarsened horizontal resolutions.

2 Model description

We use Modular Ocean Model version 6 (MOM6; Adcroft et al., 2019) for the numerical experiments. MOM6 uses an Arakawa C-grid for discretization in the horizontal direction. For the experiments in this work, we apply a global tri-polar grid with various numerical resolutions. MOM6 adopts generalized vertical coordinates with vertical Lagrangian remapping. In this work, we focus on the barotropic tides and therefore only one layer is used. A barotropic-baroclinic split time stepping scheme is used in MOM6 (Hallberg, 1997; Hallberg & Adcroft, 2009). The split time stepping allows for the solution of linearized momentum and continuity equations in the short barotropic time steps, and effectively reduces the time interval of calculating other forcing terms in the momentum equation, including the nonlinear advection, viscosity and SAL terms. Therefore, although split time stepping is designed to relax time step constraints in multi-layer simulations, it also benefits the computational cost of one-layer runs.

MOM6 is capable of simulating wetting and drying, i.e. allowing land cells with a "depth" above sea level to be flooded and ocean cell thickness to vanish. Wetting and drying effectively allow the locations of the coastlines to vary over time, which can be potentially important for the tides.

Our simulations are driven by the astronomical forcing of the principal lunar semidiurnal tide M_2. The equilibrium tide η_{EQ} is expressed in Equation 1 (e.g. Arbic et al., 2018).

$$\eta_{EQ}(\lambda, \theta) = (1 + k_2 - h_2) f(t_{\mathrm{ref}}) A \cos^2(\phi) \cos[\omega(t - t_{\mathrm{ref}}) + 2\lambda + \chi(t_{\mathrm{ref}}) + \nu(t_{\mathrm{ref}})] \quad (1)$$

Here, A is the astronomical forcing amplitude and ω is the frequency. k_2 and h_2 are the degree-two Love numbers accounting for the changes in gravitational potential field and seafloor deformations, respectively, associated with the solid earth body tides (the direct response of the solid earth to the astronomical tidal potential). $\chi(t_{\mathrm{ref}})$ is an astronomical argument that is a function of the solar and lunar positions at reference time t_{ref}. $f(t_{\mathrm{ref}})$ and $\nu(t_{\mathrm{ref}})$ are nodal correction factors to the amplitude and phase, respectively, due to low frequency tidal constituents that are often dropped in tidal simulations and that modulate larger tidal constituents such as M_2. ϕ and λ are latitude and longitude, respectively. To simplify, we use an idealized calendar at time zero, i.e.

166 we set t_{ref} and $\chi(t_{\text{ref}})$ to zero, and ignore the nodal correction factors. These simplifi-

167 cations do not affect the conclusions of our work here, as long as the corresponding har-

168 monic analysis is simplified in the same manner.

169 The energy input from astronomical forcing is balanced by dissipation due to both

170 horizontal and vertical viscous terms. For the horizontal closure, we use a biharmonic

171 form friction with Smagorinsky viscosity (Griffies & Hallberg, 2000). The primary dis-

172 sipation of barotropic tides is conducted by two types of vertical viscosity. Firstly, a quadratic

173 bottom boundary layer drag, calculated implicitly, is mainly responsible for tidal dissi-

174 pations in shallow shelf regions where tidal velocities are often as large as 1 m/s. Sec-

175 ondly, a parameterized linear topographic wave drag is included to represent dissipation

176 by breaking internal tides, a process that is absent in barotropic simulations. We use the

177 wave drag scheme by Jayne and St. Laurent (2001) (see Appendix B for more details).

178 Here, wave drag is calculated implicitly in the barotropic solver as a part of the barotropic

179 momentum equation. Acceleration due to the drag is then added explicitly to the baro-

180 clinic mode. The linear wave drag contains a tunable non-dimensional coefficient, used

181 to optimize the global tides. For most simulations in the paper, this coefficient is the only

182 tunable parameter.

183 For fast-evolving motions such as the tides, the SAL effect must be taken into con-

184 sideration. The SAL is often calculated via spherical harmonic transforms of the global

185 bottom pressure anomaly, with their spherical harmonic components multiplied by a scaled

186 factor (Equation 2).

$$p_{\text{SAL}}(\lambda, \theta) = \sum_{n=0}^{N} \sum_{m=-n}^{n} \frac{3}{\rho_e(2n+1)} (1 + k'_n - h'_n) \widetilde{\Delta p_{\text{bot}}}^{(n,m)} Y^{(n,m)}(\lambda, \theta) \qquad (2)$$

187 Here, $Y^{(n,m)}$ the spherical harmonic with degree n and order m. $\widetilde{\Delta p_{bot}}^{(n,m)}$ is the

188 corresponding spherical harmonic component of bottom pressure anomaly. ρ_e is density

189 of solid Earth. k'_n and h'_n are load Love numbers with degree n, representing seawater

190 load induced changes in gravitational potential field and seafloor deformations, respec-

191 tively. N is the highest degree used to calculate SAL. For barotropic simulations, bot-

192 tom pressure anomaly can be reduced to a linear function of SSH anomaly, i.e., $\widetilde{\Delta p_{\text{bot}}}^{(n,m)} =$

193 $\rho_0 g \widetilde{\eta}^{(n,m)}$ and $p_{\text{SAL}} = \rho_0 g \eta_{\text{SAL}}$, where g is gravitational acceleration, ρ_0 is average sea-

194   water density, $\widetilde{\eta}^{(n,m)}$ is degree-n and order-m spherical harmonic component of SSH anomaly,

195   and η_{SAL} is SSH anomaly equivalent of SAL effect.

196   An inline SAL calculation following Equation 2 is implemented in MOM6 with sim-

197   ilar algorithms as in Brus et al. (2023). Following Brus et al. (2023), we use $N = 40$

198   for barotropic tide experiments. For our baseline $0.04°$ global barotropic case, inline SAL

199   increased the total computational cost by 20% and, as a fraction of the total, this would

200   be significantly reduced in baroclinic cases that typically have O(50) levels. Inline SAL

201   method leads to the most accurate tides in almost all of our numerical experiments. A

202   comparison of inline SAL and two traditionally used SAL schemes (scalar approxima-

203   tion and read-in method) is discussed in Appendix C.

204   We run all numerical experiments with a duration of 20 model days, allowing the

205   global barotropic tides to reach equilibrium. We use the SSH from day 18 to 20 for har-

206   monic analysis and compare the results with observations.

3   Methods and experiment design

3.1   Model validation metrics

209   We use an observationally-based data-assimilative barotropic tide product TPXO

210   (Egbert & Erofeeva, 2002) version 9 as our reference for tides in the real ocean. For a

211   grid point at (λ, θ) and at given time t, we obtain from harmonic analysis of SSH the

212   M_2 constituent driven sea surface elevation, $h(\lambda, \theta, t) = \mathrm{Re}[A(\lambda, \theta) \exp\{i[\omega t - \phi(\lambda, \theta)]\}]$.

213   Here, A is the amplitude and ϕ is the phase of the tide, respectively. Mean squared er-

214   rors (MSE), $\epsilon^2(\lambda, \theta)$, of the sea surface elevation h between the model output and TPXO

215   (subscripts m and o, respectively) are calculated as in Equation 3a to quantify the model's

216   deviation from observations. Here, T is the time period of a tidal cycle. Further, the MSE

217   ϵ^2 can be decomposed into contributions from amplitude ϵ_a^2 and phase ϵ_p^2 (Shriver et al.,

218   2012), shown as the two terms in Equation 3b. For the rest of the paper, we show on maps

219   the square-root of MSE, ϵ, and its decompositions ϵ_a and ϵ_p, with the unit of height.

$$\epsilon^2(\lambda, \theta) = \frac{1}{T} \int_0^T [h_m(\lambda, \theta, t) - h_o(\lambda, \theta, t)]^2 dt \tag{3a}$$

$$= \underbrace{0.5(A_m - A_o)^2}_{\epsilon_a^2(\lambda,\theta)} + \underbrace{A_m A_o[1 - \cos(\phi_m - \phi_o)]}_{\epsilon_p^2(\lambda,\theta)} \tag{3b}$$

220   We evaluate the overall performance of each experiment with the root mean square

221 (RMS) of the globally averaged MSE. To reduce potential observation errors from the

222 satellite in coastal and polar regions, we confine the definition of "global average" to within

223 the latitudes 66°S and 66°N and depths larger than 1000 m (Arbic et al., 2004).

3.2 Baseline experiments

225   We start off with a baseline experiment having a nominal horizontal resolution of

226 0.04° and use it as a benchmark. This baseline experiment serves as the "truth" of the

227 subsequent experiments and presumably has the smallest RMS errors for the M_2 tide.

228 The only external inputs to the model are topography (see below) and prescribed wave

229 drag piston velocity (see Appendix B).

230   The topography of the baseline case is generated from the 30-second GEBCO_08

231 20091120 global dataset by taking a 5×5 average at each 0.04° tripolar grid point with

232 the minimum depth set to be above sea level and can therefore be flooded. This is fur-

233 ther smoothed with a 2D 1-2-1 smoother except near the coastline ($-5\ m$). Finally, Antarc-

234 tic ice shelves are "sunk" so that the bathymetry under ice shelves represents the wa-

235 ter there. Ice shelves are taken from a 1/2 by 1/4 degree version of BEDMAP1 (Lythe

236 & Vaughan, 2001). The datasets going into the bathymetry are relatively old because

237 this is a version of the US Navy's GOFS 3.5 (Metzger et al., 2020) bathymetry, although

238 the latter has the coastline at 0.1 m and has additional manual edits in some regions.

239   We use the 0.04° topography from this run as a source for generating sub-grid scale

240 topography in all subsequent numerical experiments. In other words, coarser resolution

241 experiments do not receive topographic details beyond the topography dataset used in

242 the baseline run. In theory, the baseline run should be the upper bound of the accuracy

243 of the tides.

3.3 Coarsened horizontal resolutions

245   To quantify tidal simulation performance change in lower resolutions, we coarsen

246 the grid of 0.04° simulations by a series of factors. By choosing integer factors, we guar-

247 antee that grid cell walls in coarsened resolutions are simply concatenations of grid cell

248 walls in the baseline run, thus simplifying implementation of porous barriers. Resolu-

249 tions of the numerical experiments vary from 0.04° to 0.36° (Table 1). Along with the

Table 1.   List of experiment resolutions. nx and ny refer to the number of grid points in the x (nominally zonal) and y (nominally meridional) directions.

number of grid cells ($nx \times ny$)	nominal resolution
9000×7056	$0.04°$
4500×3528	$0.08°$
3000×2352	$0.12°$
1500×1176	$0.24°$
$1000 \times\ 784$	$0.36°$

250   grid, the datasets for input topography, wave drag piston velocity is also weighted av-

251   eraged (by cell area) to serve as inputs for the coarsened resolution simulation.

252   In the coarsened topography, shoreline configuration, essential for both local and

253   remote tides, is inevitably modified. The locations of the model's discretized coastline

254   depend heavily on the criterion for qualifying a grid cell in the coarsened resolution as

255   an ocean cell. In the simplest scenario, we can arbitrarily choose a cutoff ratio of the ocean

256   area in the coarsened cells ranging from 0 to 1, where 0 results in more ocean cells and

257   therefore more landward retreated coastlines while 1 gives more seaward moving coast-

258   lines. Without a better argument to support either the "more ocean" or "more land"

259   coastlines, we use 50% as our cutoff for ocean cells.

260   Following previous works (Egbert et al., 2004; Buijsman et al., 2015, 2020), the lin-

261   ear wave drag is re-tuned for different horizontal resolutions, as well as different SAL schemes.

262   The globally averaged SSH RMS error is used as the criterion to decide the optimal non-

263   dimensional coefficient for the linear wave drag at each resolution.

264   **3.4 Porous barriers**

265   *3.4.1 Implementation*

266   Effectively, porous barriers constrain transport across the vertical walls of grid cells,

267   thus avoiding the overly-widened pathways between cells. This is achieved by including

268   a non-dimensional factor that approximates the openness of the grid cell widths used for

²⁶⁹ calculating transport. The discretized continuity equation in the model can be approx-

²⁷⁰ imated as

$$h^{n+1} = h^n + \frac{\Delta t}{\Delta_x \Delta_y} \cdot [\delta_x(u \cdot h_x^* \alpha_x \Delta_y) + \delta_y(v \cdot h_y^* \alpha_y \Delta_x)] \tag{4}$$

²⁷¹ Here h^n is the layer thickness at time step n, u and v are velocity components in

²⁷² the x and y direction, respectively, h^* stands for the effective thickness at the velocity

²⁷³ points, Δ_x and Δ_y are the time-invariant grid cell widths in the x and y direction, re-

²⁷⁴ spectively, Δt is the time step size, and α_x and α_y are the non-dimensional factors from

²⁷⁵ porous barriers, which are smaller than or equal to 1.

²⁷⁶ At each time step, the non-dimensional factors α_x and α_y, located at velocity cells

²⁷⁷ (i.e. grid cell walls in C-grid models), are determined by two aspects, a prescribed lo-

²⁷⁸ cal topography vertical profile (discussed in the next section), and the height where the

²⁷⁹ layer interfaces intercept this profile. For MOM6, the time-variant layer interface height

²⁸⁰ is usually calculated at tracer cells (i.e. grid cell centers in C-grid models), and there-

²⁸¹ fore additional steps are needed to evaluate the interface height at the velocity points.

²⁸² For simplicity, we use the arithmetic mean of the interface heights of the velocity point's

²⁸³ neighbor cells.

²⁸⁴ ### 3.4.2 Topography profiles at velocity points

²⁸⁵ The prescribed local topography vertical profiles are constructed by statistical pa-

²⁸⁶ rameters from high resolution datasets. Following Adcroft (2013), we use three param-

²⁸⁷ eters: shallowest, deepest and mean depths at the cell walls, to form a simple idealized

²⁸⁸ V-/U-shape depth profile, which infers sub-grid scale features.

²⁸⁹ From the baseline topography, we calculate ocean depths at grid cell walls by in-

²⁹⁰ terpolating from those at the centers of adjacent grid cells. There are multiple choices

²⁹¹ of interpolation methods, and the best choice is probably specific to the problem being

²⁹² addressed. For instance, for a hydrologically-controlled downward flow in a channel, us-

²⁹³ ing the shallowest depth of adjacent cells may better describe the problem. The direc-

²⁹⁴ tions of tidal flow reverse constantly, such that the basin shape and therefore the tidal

²⁹⁵ resonance is perhaps more important. Therefore we use a simple average of the adjacent

²⁹⁶ tracer cell depths here.

Figure 2. Illustration of the method for generating the depth profiles at grid cell walls. From a high-resolution topography dataset (left panel), we can calculate the wall depth with a simple arithmetic mean (numbers in white color) from neighboring cell center depths (numbers in grey color). When horizontal resolution is coarsened (right panel), an area-weight average is used to obtain the new cell center depths, while a range of depths at new walls (numbers in the brackets in white color) is given. The statistics of these depths (e.g. maximum, minimum and mean) can be used to generate a simple-shaped profile. Note that grid cell numbers in the baseline case are always multiples of grid cell numbers in coarsened resolutions, making the new walls in coarse resolutions always concatenations of the old walls in the baseline case.

We can then generate topography profiles for coarsened resolutions using this $0.04°$ map of topography at the walls. For each coarsened resolution, the shallowest, deepest and mean depths are obtained from the grid cell walls of the $0.04°$ resolution that constitute new walls in the new resolution (Figure 2). For instance, at the $0.12°$ resolution, which is constructed by aggregating 3×3 grid cells from the $0.04°$ configuration, there are three depth values at the grid cell walls at each direction; and the maximum, minimum and mean of these three values are used as parameters to construct the depth profile. Note that by design, the numbers of grid cells of the baseline run in both directions are always multiples of the number in the low resolution runs, therefore the grid cell walls in the low resolution always coincide the grid cell walls in the baseline run. It is worth mentioning that the shallowest, deepest and mean depths (i.e. D_{shallow}, D_{mean} and D_{deep} in Figure 1) are determined only by sub-grid scale depth values at grid cell walls, not by cell center depth values. For each coarsened resolution, the depth profiles at the walls are uncorrelated to depths in their nearby tracer cells. The depth profiles are additional degrees of freedom inherited from the baseline topography.
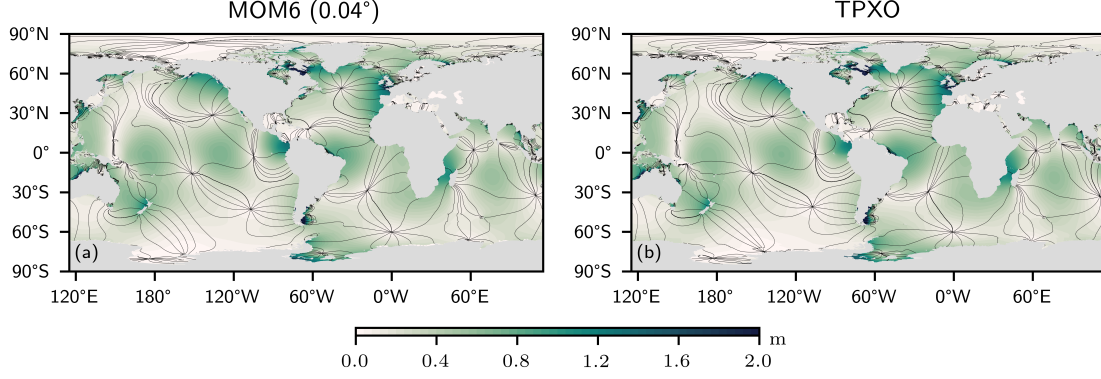
Figure 3. Maps of M_2 surface tide amplitude (colors) and phase (contours) from MOM6 (a) and TPXO atlas (Egbert & Erofeeva, 2002) (b). Phase contours have an interval of $30°$. The MOM6 maps are from the baseline experiment, which has a nominal $0.04°$ horizontal resolution and uses inline SAL.

4 Results: Sensitivity to horizontal resolutions

4.1 Tides from the baseline experiment

We show amplitude and phase of SSH induced by M_2 tides from the baseline experiment in MOM6 (Figure 3a) and compare modeled SSH fields with observations (Figure 3b). The non-dimensional linear wave drag coefficient is 0.8, which gives the smallest global RMS tidal error. Visually, the spatial distribution of the amplitude and phase match with the real ocean tides. A quantitative comparison between the model and observations is shown in Figure 4a. Overall, the $0.04°$ resolution MOM6 simulation has an RMS error of 3.74 *cm* in the deep ocean outside of high latitudes. This is to be compared with previous results such as 5 *cm* in Egbert et al. (2004), 4.4 *cm* in Schindelegger et al. (2018), 1.94 *cm* in Blakely et al. (2022) and 6.8 *cm* in Barton et al. (2022). The SSH error is mostly dominated by tides in the Atlantic basin, possibly related to the strongly resonant tides in the Hudson Bay (Arbic et al., 2007, 2009). In the Pacific and Indian Oceans, tidal errors are comparatively weaker but are still noticeable near the high tides areas between the amphidromic points.

The total error at each grid point is further decomposed into contributions from amplitude (Figure 4b) and phase (Figure 4c). The large Atlantic errors are mostly attributed to the phase term. For cotidal lines near the counterclockwise amphidromic points in the Atlantic, MOM6 is leading in phase to TPXO. This phase offset, multiplied by
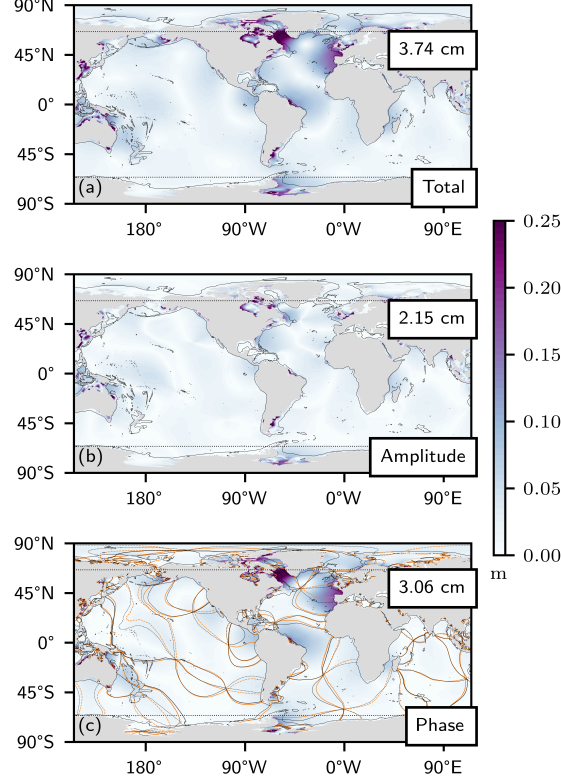
Figure 4. Maps of the square-root of MSE ϵ of SSH between the baseline experiment in MOM6 and TPXO (a) and decomposition into contributions from amplitude ϵ_a (b) and phase ϵ_p (c). Cotidal lines from MOM6 (orange) and TPXO (dark grey) are overlaid in (c) for comparison. Numbers on maps show averaged RMS error over the deep ocean and outside of high latitudes. Contours of $1000\ m$ depth are shown in light grey curves and the latitudes of $66°$N and $66°$S are shown in dotted grey lines, which delineate the deep-ocean area over which RMS errors are computed.

331   large amplitude, results in large phase errors. Similar phase offsets between model and

332   observations can be found in some other places, but the phase error contributions are

333   weak with a low tidal amplitude (see Equation 3b).

334   Tides are sensitive to locations of coastlines, which undergo constant changes in

335   the real ocean due to flood and ebb tides. Therefore we also test the effect of allowing

336   wetting and drying in the baseline configuration. The global tidal error reduction is about

337    $0.02\ cm$ at the $0.04°$ resolution. This reduction indicates that while changing coastlines

338   does have an effect on open ocean tides, the resulting effect is much smaller than the ef-

339 fects of porous barriers that we focus on in this work (as we show in the following). Nonethe-

340 less, we adopt wetting and drying in all of our numerical experiments.

4.2 The effect of horizontal resolution

342 We next investigate how tidal errors change as a function of horizontal resolution.

343 To obtain the smallest RMS error, the linear wave drag is re-tuned for each run with a

344 new resolution. It is found that the non-dimensional coefficient needs to increase at lower

345 resolutions. The averaged RMS errors of tidal SSH from coarsened resolution experiments

346 are shown in Figure 5 (solid curves, the dashed curves are discussed later in Section 5.2).

347 Tidal errors increase almost linearly with decreased horizontal resolution, consistent with

348 results in previous studies (e.g. Egbert et al., 2004).

349 The decomposition of the total error suggests that the phase error increases faster

350 than the amplitude error as resolution is decreased, such that phase error makes the greater

351 contribution to higher tidal SSH errors at low resolutions. The change in tidal ampli-

352 tude is directly associated with tidal energetics. Tidal currents are usually weaker with

353 lower resolution horizontal grids, which would change tidal dissipation and energy in-

354 put. The phase, on the other hand, is also affected by propagations and reflections of

355 the shallow-water gravity waves. When horizontal resolution is coarsened, the model to-

356 pography also changes. It is likely that the geographic locations of cotidal lines and am-

357 phidromic points are changed due to the changes of ocean basin geometries.

358 The spatial distribution of the increased errors in low resolution runs is exempli-

359 fied by the 0.36° case in Figure 6. The RMS error increase is not uniform across ocean

360 basins. The greatest differences appear in the Pacific and Indian Oceans, where tidal er-

361 rors in the baseline case are small. We decompose the total MSE to contributions from

362 each basin in Figure 7. While tidal errors change monotonically across resolutions in al-

363 most all ocean basins, the increase in the Pacific, Indian and Southern Oceans are par-

364 ticularly large, especially in the two lowest resolution cases. In particular, the Pacific basin

365 is the primary driver of tidal error increases at low resolutions, largely due to the phase

366 error (Figure 6c).

367 It is also worth mentioning that there are regions in which the tidal errors decrease

368 at lower resolutions, notably in the region north of New Zealand, and in some parts of
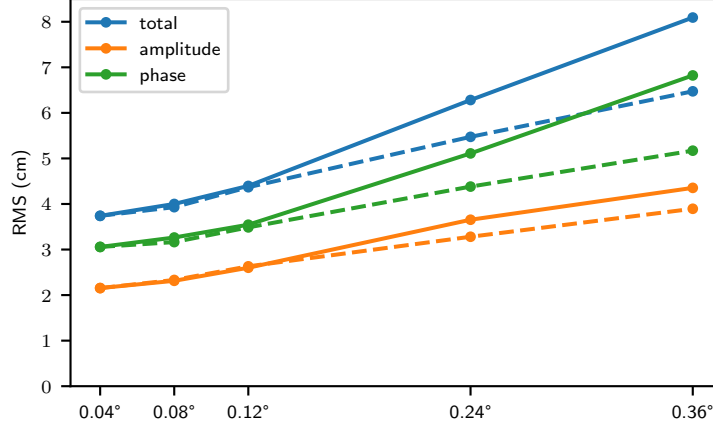
369 the Atlantic basin including Hudson Bay.

Figure 5. Globally averaged RMS errors for M_2 tides as a function of horizontal resolution. RMS errors are calculated over the deep ocean and outside of high latitudes. The total error (blue) is decomposed into contributions from amplitude (orange) and phase (green). Solid curves show results from control experiments in which topography is simply coarsened (discussed in Section 4.2) and dashed curves show results from the same setup with porous barriers implemented (discussed in Section 5.2).

5 Results: the effect of porous barriers

5.1 Local implementation

As discussed in Section 3.4.1, porous barriers effectively narrow grid cell in coarse resolutions. Therefore, if implemented at choke points between a marginal sea and the open ocean, porous barriers will modify the connectivity in that place, potentially changing tides in remote deep oceans. We add porous barriers near the Hudson Strait (Figure 8a) at the coarsest resolution (0.36°). The Hudson Strait connects the Hudson Bay, with high tides and dissipation rates (Egbert & Ray, 2000; Cummins et al., 2010), to the open ocean of the North Atlantic; it has been shown to be one of the key locations where topography can influence both local and remote tides. As shown in Figure 8b, the tidal errors become worse with porous barriers implemented at the mouth of Hudson Strait. The changes in the tidal SSH extends from the Labrador Sea to the entire Atlantic basin, and reach as far as the western Pacific through the Indian Ocean. This result highlights the role that marginal seas play in the deep ocean tides. The response in tidal errors here is rather similar to the findings in Arbic et al. (2009), in which the Hudson Strait is com-
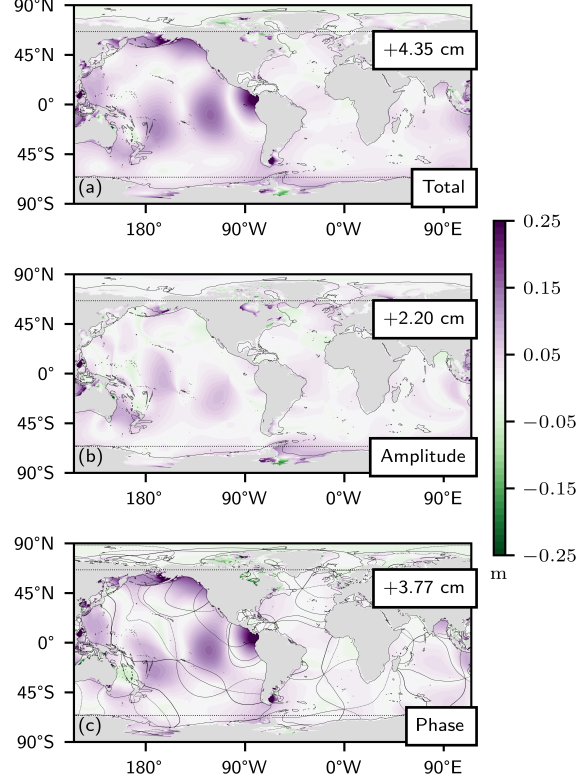
Figure 6. Maps of changes in square-root of MSE ϵ and its amplitude ϵ_a and phase ϵ_p components between $0.36°$ resolution and the baseline experiment $(0.04°)$. Numbers on maps show changes of globally averaged RMS error. Cotidal lines from the baseline experiment are overlaid in (c) to help locate the changes.
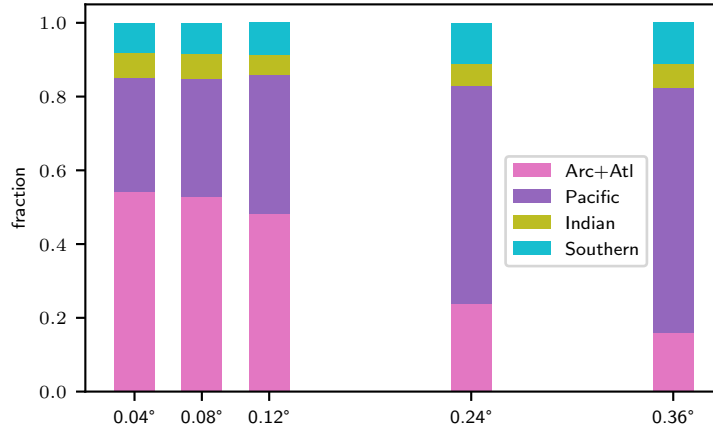

Figure 7. Relative contribution of each ocean basin to the total MSE (without porous barriers) at each resolution. Divided ocean basins: Atlantic and Arctic Oceans (pink), Pacific Ocean (purple), Indian Ocean (olive) and Southern Ocean (cyan).
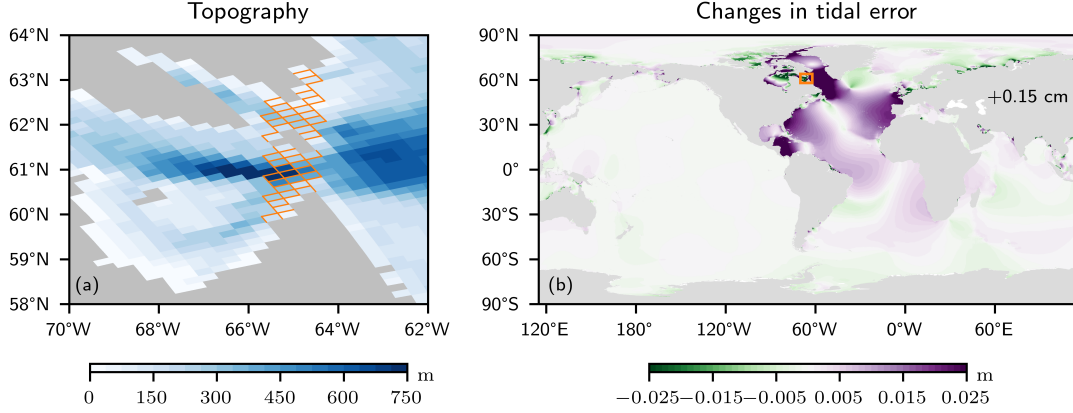
Figure 8. (a): Topography near the mouth of Hudson Strait (shaded color) and grid points where porous barriers are applied (orange lines) at 0.36° resolution. (b): Changes in total tidal error at 0.36° resolution due to local implementation of porous barriers at Hudson Strait. The orange box shows the location of the map in (a).

pletely blocked in one of their experiments. We speculate the large tidal errors in the Atlantic from the baseline experiment (Figure 4) could be associated with relatively inadequate topography representations near the Hudson Strait; and porous barriers do nothing but reintroduce these inaccurate topographic features to the coarse resolution runs (Note from Figure 6 that the coarse resolution tidal error in fact slight decreases in the Labrador Sea).

The example here demonstrated the model's sensitivity to sub-grid scale topography and the utility of porous barriers to recover some effects from unresolved topographic features. The remote response to local topography modification suggests a global implementation of porous barrier will be far more complicated. The effect of a global implementation may not be a simple summation of all the responses due to the specific local changes, as we show in the next section.

5.2 Global tidal error change

We now evaluate the effect of a global implementation of porous barriers. Porous barriers are added in each coarsened resolution and results are shown in the dashed curves in Figure 5. In all cases with coarsened horizontal resolution, the total tidal error is decreased with a global implementation of porous barriers. For instance, with the help of
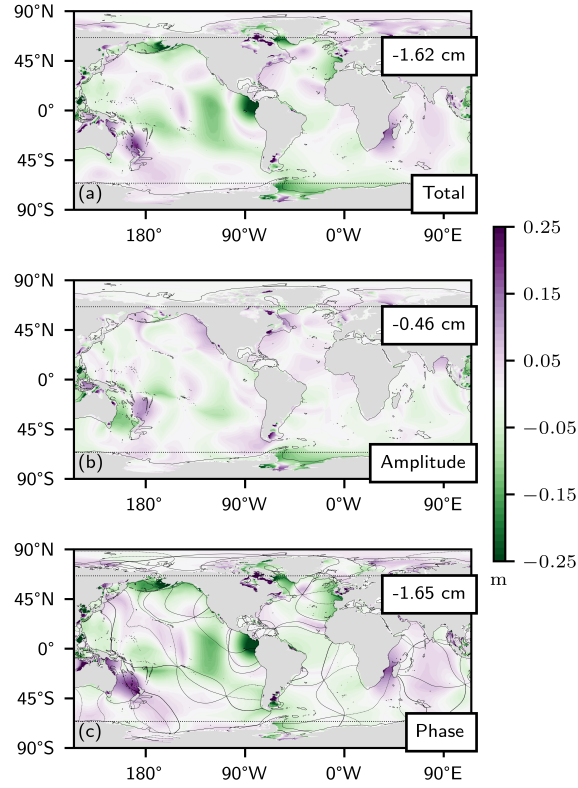
Figure 9. Maps of changes in square-root of MSE ϵ and its amplitude ϵ_a and phase ϵ_p components from the experiment with porous barriers compared with the one without at $0.36°$ resolution. Numbers on maps show changes of globally averaged RMS error.

porous barriers, the globally averaged RMS error in 0.36° case is comparable with that of the 0.24° case without porous barriers. In most cases, the reduction of tidal error results from reduction in both amplitude and phase errors. Phase error changes are greater than amplitude error changes and are therefore the more dominant factor underlying changes in total errors..

Geographically, signs and magnitudes of tidal error changes are not uniform. The overall improvement results from large and widespread tidal error reductions, but there are also places with increases of tidal error. Generally speaking, most error reductions occur in areas where the tidal error is large compared with the baseline experiment (Figure 9). The globally averaged RMS reduction is largely driven by decreases in the Pacific Ocean, both in the open ocean and along its eastern boundaries. Inversely, tidal error is increased in a number of regions. The southern Indian Ocean and an area north of New Zealand suffer from a significant large tidal error increase. The Atlantic basin overall observes a moderate change, with both signs of change present. Notably, Hudson Bay and western North Atlantic display increases of tidal errors, as with the local implementation in the previous section.

Comparing Figure 9 and Figure 6, it is obvious that porous barriers generally reverse changes arising from coarsening horizontal resolution. It significantly reduces Pacific errors but also brings back some shortcomings in the North Atlantic seen in the baseline run. In other words, porous barriers accomplish what they are intended to accomplish by introducing lost geometric features back to coarse resolutions.

5.3 Possible optimizations

Even though a local implementation of porous barriers (as in the example of Hudson Strait) may not improve the global tides, the modeled tidal response to a global implementation of porous barriers is favorable. This response suggests there could be possible tuning options to further reduce the total global tidal error. We present here a number of choices based on the configuration of our experiments.

The inhomogeneity of tidal error changes across basins prompts us to examine whether these changes are responses to local or remote implementation of porous barriers. We first explore effects of single-basin implementations of porous barriers. Results from the 0.36° case are listed in Table 2. The global tidal error is reduced for each case where porous

Table 2. Changes in global tidal error from 0.36° resolution (in cm)

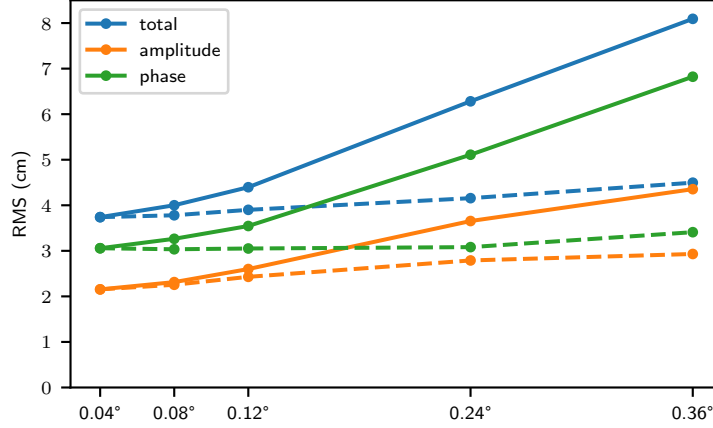| Region	Global	Atlantic+Arctic	Pacific	Indian	Southern	No Southern
$\Delta\epsilon$	-1.62	-0.19	-2.78	-0.22	-0.41	-3.03

Figure 10. Globally averaged RMS error for M_2 tides as a function of horizontal resolution. As in Figure 5 but for porous barriers implemented only north of 15°S.

barriers are applied to a single ocean. The Pacific-only implementation has the largest effect, even more effective than the global implementation. This suggests that there are cancellations between remote effects of local implementations. In addition, if we exclude the Southern Ocean, the reduction of tidal errors is the greatest, indicating the Southern Ocean's porous barriers have an negative effect on reducing tidal errors.

Inspired by this finding, we further test the dependence of improvement as a function of southern boundaries. We find that 15°S is the optimal southern boundary for implementing porous barriers, and the new configuration drastically reduces tidal errors in coarse resolution simulations (Figure 10). Compared with Figure 5, this optimization leads to further reductions in both phase and amplitude errors, with a greater change in the former. In fact, phase errors almost remain unchanged across resolutions. It is worth mentioning that the latitude 15°S excludes much of the error increases in Figure 9 (to the north of New Zealand and Indian Ocean). These results suggest possibilities of further reducing global tidal errors by tuning porous barrier implementation, but more im-

portantly the complication of the effect of local topography on physical processes of various timescales. Some speculations are provided in the following discussion section.

6 Discussions and conclusions

In this work, we study the application of porous barriers, a representation of sub-grid scale topography, to global barotropic tides. A series of experiments with various horizontal resolutions are designed. Globally averaged tidal RMS errors, referenced to the observationally-based product TPXO, increase with coarsened resolutions. The error increase is due to contributions from both amplitude and phase, with phase error changes being the relatively large factor. The geographic distribution of error changes is not uniform, which may expose shortcomings of the topography in the baseline experiment. A global implementation of porous barriers can significantly revert some of the changes from the coarsened horizontal resolution, especially phase errors.

We explore the possibility of further fine-tuning porous barriers by modifying locations of implementation. Specifically, we target regions where tidal errors are increased with porous barriers. The case with porous barriers implemented only north of 15°S results in even better tidal error reductions than a global implementation. First of all, it is possible that regions where tidal errors are increased by porous barriers are affected by the quality of local and remote topography. Second, the subtleties of Southern Ocean topography may play a certain role. For instance, simulations in this work do not include dynamical ice shelves in the Antarctica, which has been shown to impact on global tidal errors (Pal et al., 2023). Third, the optimal topography configuration may not be necessarily consistent for physical processes of various timescales and frequencies, which means different implementations may be needed depending on the focus of the simulations. For tides, rather than providing conclusive guidelines on how porous barriers should be implemented geographically, we emphasize that this exercise suggests possibilities of further refinement, in which case phase error in particular can be reduced in coarse horizontal resolution simulations.

Our experiments demonstrate the capability of porous barriers in an idealized and simple setup. Rather than extracting sub-grid scale topographic details from finer resolutions, we use topography from a chosen baseline setup (0.04° resolution) as the source for sub-grid scale topography in coarse resolution runs. This ensures that no further to-

pographic details are introduced through the addition porous barriers relative to the baseline, which is presumed to yield a lower bound of the tidal errors. In practice, porous barriers constructed from much finer resolution datasets may result in even greater improvement of tides. It is also not unreasonable to assume that the tidal errors from relatively high resolution simulations, such as the baseline case ($0.04°$ resolution), can be reduced by porous barriers using high resolution topography dataset.

The construction and implementation of porous barriers is a rather simplified version compared with Adcroft (2013) in that we are not taking into consideration the structure and connectivity within coarsened grid cells. Adcroft (2013) proposed an objective mapping method to ensure that the effect due to walls within coarsened resolution cells, which would otherwise be ignored, are incorporated into sub-grid scale structure in walls surrounding grid cells, thus avoiding the creation of deep pathways. We choose not to adopt this approach for simplicity. It is possible that with a more faithful construction of porous barriers that includes the inner cell geometries, tides at coarsened resolutions could be further improved. We leave this for possibility as a subject for future research.

Another aspect of sub-grid scale topography is the so-called "porous media", where a profile of topography at cell centers is used to constrain the volume/mass capacity of the grid cells. However, porous media do not affect fully submerged grid cells when there is only one layer in the vertical direction. As discussed in Section 4.1, we did not find the addition of wetting and drying near the coastlines to change our results significantly. Thus we conclude that porous media would not be effective in improving tides in this setup. However, porous medias could potentially be a useful complement to the porous barriers in multi-layer simulations.

Appendix A Governing shallow-water equations

Dynamics of one-layer barotropic simulations in MOM6 is governed by shallow-water equations (Equation A1 and Equation A2). Here, $\mathbf{u}$ is horizontal velocity, $f + \zeta$ is the total vertical vorticity, where f is the Coriolis parameter and $\zeta = \partial_x v - \partial_y u$ is relative vertical vorticity. η is SSH anomaly of total thickness h referenced to the resting depth of the ocean, η_{EQ} and η_{SAL} are the equilibrium tide and SAL effect, respectively (see Section 2 for their expressions). $\mathbf{F}_{quad}$ is a quadratic bottom drag and $\mathbf{F}_h$ is horizontal viscosity term. $\mathbf{F}_{wave}$ is a parameterized linear wave drag term, elaborated in Appendix B.
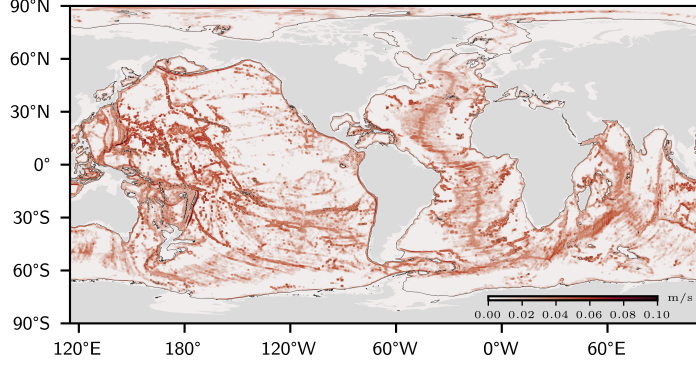
Figure B1. Map of piston velocity C_{JSL} used in Jayne and St. Laurent (2001) linear wave drag scheme. The black contours are used to denote locations of the 1000-m isobath.

$$\partial_t \mathbf{u} = -(f + \zeta)\hat{\mathbf{k}} \times \mathbf{u} - \nabla\left[\frac{1}{2}(u^2 + v^2)\right] - g\nabla(\eta - \eta_{\text{EQ}} - \eta_{\text{SAL}}) + \mathbf{F}_{\text{quad}} + \mathbf{F}_{\text{wave}} + \mathbf{F}_h \quad \text{(A1)}$$

$$\partial_t \eta = -\nabla \cdot (\mathbf{u}h) \tag{A2}$$

Appendix B   Parameterized linear wave drag for open-ocean tidal dissipation

We adopt the wave drag scheme by Jayne and St. Laurent (2001) (hereinafter, JSL). The adoption of JSL wave drag scheme in this work is similar to Buijsman et al. (2015), to which the readers are referred for more details.

In essence, the wave drag force term is expressed in Equation B1, where χ is a non-dimensional tuning parameter, $\mathbf{u}$ is ocean (barotropic) velocity, and h is total water column thickness. C_{JSL} is a pre-calculated piston velocity that is a function of both bottom roughness and bottom buoyancy frequency. A global map of C_{JSL} for the baseline case (0.04° horizontal resolution) is shown in Figure B1. Note that large C_{JSL} is located near ocean ridges and C_{JSL} is only non-zero for regions deeper than 1000 m.

$$\mathbf{F}_{\text{wave}} = \chi \frac{C_{\text{JSL}}\mathbf{u}}{h} \tag{B1}$$

Table C1. Comparison of three SAL schemes in the baseline case (0.04° horizontal resolution). The first column compares wave drag coefficients with the smallest deep-ocean tidal errors. The second columns compares total deep-ocean tidal errors and the last two columns show decompositions of the errors into amplitude and phase.

SAL scheme	Wave drag coefficient	Total (cm)	Amplitude (cm)	Phase (cm)
Inline	0.8	3.74	2.15	3.06
Scalar	1.0	5.98	3.35	4.95
Read-in	0.9	3.81	2.77	2.62

Appendix C Comparison of self-attraction and loading schemes

We show a demonstration of the utility of inline SAL in a comparison with two other types of SAL schemes used in previous studies: a scalar approximation (Accad & Pekeris, 1978), in which the SAL is simply a fraction of the SSH anomaly and a read-in method, in which time-invariant amplitudes and phases of the M_2 tidal SAL from observationally-based dataset are provided to the models. Inline SAL is more accurate than the scalar approximation because the latter does not account for the scale-selective nature of SAL. In contrast to read-in SAL, inline SAL can be used in studies of past and future tides, in which the tides and their SAL signal have changed significantly. The iterative method, where the ocean model is run repeatedly to get a converged off-line SAL, can also be used for past and future tides, but we exclude it from our tests in this paper because it offers no advantages over inline SAL.

We first compare the results from the baseline simulation in Table C1. For each SAL scheme, wave drag coefficients are re-tuned and listed in the leftmost column of Table C1. The scalar approximation results in much larger tidal errors than inline SAL. Tidal errors from inline SAL are comparable to these from read-in SAL, which uses observed tidal SAL amplitudes and phases as inputs to the model. Read-in SAL, however, is not applicable to non-periodic motions; moreover, it removes the dynamical feedbacks between bottom pressure anomaly and the SAL term and is therefore incapable of handling the changing tides in climate change scenarios. Due to the obvious advantages in small tidal errors and dynamical justifications, we argue that inline SAL should be the top choice for global tidal simulations.
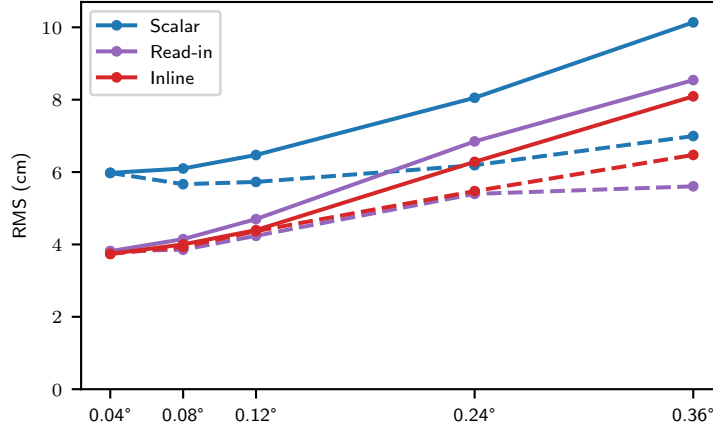
Figure C1. Globally averaged total RMS error for M_2 tides as a function of horizontal resolution for different SAL options. Solid curves show results from control experiments in which topography is simply coarsened and dashed curves show results from the same setup with porous barriers implemented.

Next, experiments with coarsened horizontal resolutions and their corresponding experiments with porous barriers are repeated with two other SAL schemes in Figure C1. Consistent with the comparison of the baseline cases, inline SAL results in the most accurate tides for all resolutions (solid curves). The superior performance of inline SAL in lower resolutions over the read-in method suggests the importance of SAL's dynamical interaction. With porous barriers (dashed curves), all SAL schemes show considerable improvement of tidal errors in coarsened resolution simulations, which provides supports to the robustness of results on the utility of porous barriers.

Open Research

The version of MOM6 source code used in all simulations of this work can be found at `https://github.com/herrwang0/MOM6/releases/tag/paper_porousbarriers`. Runtime parameters, input files for the model, and output from all simulations in this work is stored at Wang et al. (2023) (`https://doi.org/10.5281/zenodo.8166251`).

Acknowledgments

We would like to thank Alistair Adcroft and Theresa Morrison for internal reviews of the paper. A first version of porous barriers in MOM6 is coded by Sam Ditkovsky, which

References

Accad, Y., & Pekeris, C. L. (1978). Solution of the tidal equations for the M_2 and S_2 tides in the world oceans from a knowledge of the tidal potential alone. *Philosophical Transactions of the Royal Society of London. Series A, Mathematical and Physical Sciences*, *290*(1368), 235–266.

Adcroft, A. (2013). Representation of topography by porous barriers and objective interpolation of topographic data. *Ocean Modelling*, *67*, 13–27.

Adcroft, A., Anderson, W., Balaji, V., Blanton, C., Bushuk, M., Dufour, C. O., . . . others (2019). The GFDL global ocean and sea ice model OM4.0: Model description and simulation features. *Journal of Advances in Modeling Earth Systems*, *11*(10), 3167–3211.

Arbic, B. K. (2022). Incorporating tides and internal gravity waves within global ocean general circulation models: A review. *Progress in Oceanography*, 102824.

Arbic, B. K., Alford, M. H., Ansong, J. K., Buijsman, M. C., Ciotti, R. B., Farrar, J. T., . . . others (2018). Primer on global internal tide and internal gravity wave continuum modeling in HYCOM and MITgcm. *New frontiers in operational oceanography*, 307–392.

Arbic, B. K., Garner, S. T., Hallberg, R. W., & Simmons, H. L. (2004). The accuracy of surface elevations in forward global barotropic and baroclinic tide models. *Deep Sea Research Part II: Topical Studies in Oceanography*, *51*(25-26), 3069–3101.

Arbic, B. K., & Garrett, C. (2010). A coupled oscillator model of shelf and ocean tides. *Continental Shelf Research*, *30*(6), 564–574.

Arbic, B. K., Karsten, R. H., & Garrett, C. (2009). On tidal resonance in the global ocean and the back-effect of coastal tides upon open-ocean tides. *Atmosphere-Ocean*, *47*(4), 239–266.

Arbic, B. K., St-Laurent, P., Sutherland, G., & Garrett, C. (2007). On the resonance and influence of the tides in Ungava Bay and Hudson Strait. *Geophysical Research Letters*, *34*(17).

Arbic, B. K., Wallcraft, A. J., & Metzger, E. J. (2010). Concurrent simulation of the eddying general circulation and tides in a global ocean model. *Ocean Modelling*, *32*(3-4), 175–187.

Barton, K. N., Pal, N., Brus, S. R., Petersen, M. R., Arbic, B. K., Engwirda, D., ... Schindelegger, M. (2022). Global barotropic tide modeling using inline self-attraction and loading in MPAS-Ocean. *Journal of Advances in Modeling Earth Systems*, *14*(11), e2022MS003207.

Blakely, C. P., Ling, G., Pringle, W. J., Contreras, M. T., Wirasaet, D., Westerink, J. J., ... others (2022). Dissipation and bathymetric sensitivities in an unstructured mesh global tidal model. *Journal of Geophysical Research: Oceans*, *127*(5), e2021JC018178.

Brus, S. R., Barton, K. N., Pal, N., Roberts, A. F., Engwirda, D., Petersen, M. R., ... Schindelegger, M. (2023). Scalable self attraction and loading calculations for unstructured ocean tide models. *Ocean Modelling*, 102160.

Buijsman, M. C., Arbic, B. K., Green, J., Helber, R. W., Richman, J. G., Shriver, J. F., ... Wallcraft, A. (2015). Optimizing internal wave drag in a forward barotropic model with semidiurnal tides. *Ocean Modelling*, *85*, 42–55.

Buijsman, M. C., Stephenson, G. R., Ansong, J. K., Arbic, B. K., Green, J. M., Richman, J. G., ... Zhao, Z. (2020). On the interplay between horizontal resolution and wave drag and their effect on tidal baroclinic mode waves in realistic global ocean simulations. *Ocean Modelling*, *152*, 101656.

Clarke, A. J. (1991). The dynamics of barotropic tides over the continental shelf and slope. In B. B. Parker (Ed.), *Tidal hydrodynamics* (pp. 79–108). John Wiley and Sons.

Cummins, P. F., Karsten, R. H., & Arbic, B. K. (2010). The semi-diurnal tide in Hudson Strait as a resonant channel oscillation. *Atmosphere-ocean*, *48*(3), 163–176.

Egbert, G. D., & Erofeeva, S. Y. (2002). Efficient inverse modeling of barotropic ocean tides. *Journal of Atmospheric and Oceanic technology*, *19*(2), 183–204.

Egbert, G. D., & Ray, R. D. (2000). Significant dissipation of tidal energy in the deep ocean inferred from satellite altimeter data. *Nature*, *405*(6788), 775–778.

Egbert, G. D., & Ray, R. D. (2001). Estimates of M_2 tidal energy dissipation from TOPEX/Poseidon altimeter data. *Journal of Geophysical Research: Oceans*, *106*(C10), 22475–22502.

Egbert, G. D., Ray, R. D., & Bills, B. G. (2004). Numerical modeling of the global semidiurnal tide in the present day and in the last glacial maximum. *Journal*

631   *of Geophysical Research: Oceans*, *109*(C3).

632   Garrett, C. (1972). Tidal resonance in the Bay of Fundy and Gulf of Maine. *Nature*,

633   *238*(5365), 441–443.

634   Griffies, S. M., & Hallberg, R. W. (2000). Biharmonic friction with a Smagorinsky-

635   like viscosity for use in large-scale eddy-permitting ocean models. *Monthly*

636   *Weather Review*, *128*(8), 2935–2946.

637   Hallberg, R. (1997). Stable split time stepping schemes for large-scale ocean model-

638   ing. *Journal of Computational Physics*, *135*(1), 54–65.

639   Hallberg, R., & Adcroft, A. (2009). Reconciling estimates of the free surface height

640   in lagrangian vertical coordinate ocean models with mode-split time stepping.

641   *Ocean Modelling*, *29*(1), 15–26.

642   Heath, R. (1981). Estimates of the resonant period and Q in the semi-diurnal tidal

643   band in the north atlantic and pacific oceans. *Deep Sea Research Part A.*

644   *Oceanographic Research Papers*, *28*(5), 481–493.

645   Hendershott, M. (1972). The effects of solid earth deformation on global ocean tides.

646   *Geophysical Journal International*, *29*(4), 389–402.

647   Jayne, S. R., & St. Laurent, L. C. (2001). Parameterizing tidal dissipation over

648   rough topography. *Geophysical Research Letters*, *28*(5), 811–814.

649   Lythe, M. B., & Vaughan, D. G. (2001). BEDMAP: A new ice thickness and sub-

650   glacial topographic model of antarctica. *Journal of Geophysical Research: Solid*

651   *Earth*, *106*(B6), 11335–11351.

652   Metzger, E., Hogan, P., Shriver, J., Thoppil, P., Douglass, E., Yu, Z., ... others

653   (2020). *Validation test report for the global ocean forecast system 3.5-1/25*

654   *degree HYCOM/CICE with tides* (Tech. Rep.). Navel Research Laboratory,

655   Washington DC, United States.

656   Müller, M. (2007). The free oscillations of the world ocean in the period range 8 to

657   165 hours including the full loading effect. *Geophysical research letters*, *34*(5).

658   Müller, M., Haak, H., Jungclaus, J. H., Sündermann, J., & Thomas, M. (2010). The

659   effect of ocean tides on a climate model simulation. *Ocean Modelling*, *35*(4),

660   304–313.

661   Pal, N., Barton, K. N., Petersen, M. R., Brus, S. R., Engwirda, D., Arbic, B. K., ...

662   Wirasaet, D. (2023). Barotropic tides in MPAS-Ocean (E3SM V2): impact of

663   ice shelf cavities. *Geoscientific Model Development*, *16*(4), 1297–1314.

Platzman, G. W., Curtis, G. A., Hansen, K. S., & Slater, R. D. (1981). Normal modes of the world ocean. part II: Description of modes in the period range 8 to 80 hours. *Journal of Physical Oceanography*, *11*(5), 579–603.

Ray, R. (1998). Ocean self-attraction and loading in numerical tidal models. *Marine Geodesy*, *21*(3), 181–192.

Schiller, A., & Fiedler, R. (2007). Explicit tidal forcing in an ocean general circulation model. *Geophysical research letters*, *34*(3).

Schindelegger, M., Green, J., Wilmes, S.-B., & Haigh, I. D. (2018). Can we model the effect of observed sea level rise on tides? *Journal of Geophysical Research: Oceans*, *123*(7), 4593–4609.

Shihora, L., Sulzbach, R., Dobslaw, H., & Thomas, M. (2022). Self-attraction and loading feedback on ocean dynamics in both shallow water equations and primitive equations. *Ocean Modelling*, *169*, 101914.

Shriver, J., Arbic, B. K., Richman, J., Ray, R., Metzger, E., Wallcraft, A., & Timko, P. (2012). An evaluation of the barotropic and internal tides in a high-resolution global ocean circulation model. *Journal of Geophysical Research: Oceans*, *117*(C10).

Thomas, M., Sündermann, J., & Maier-Reimer, E. (2001). Consideration of ocean tides in an OGCM and impacts on subseasonal to decadal polar motion excitation. *Geophysical Research Letters*, *28*(12), 2457–2460.

Vinogradova, N. T., Ponte, R. M., Quinn, K. J., Tamisiea, M. E., Campin, J.-M., & Davis, J. L. (2015). Dynamic adjustment of the ocean circulation to self-attraction and loading effects. *Journal of Physical Oceanography*, *45*(3), 678–689.

Wang, H., Hallberg, R. W., Wallcraft, A. J., Arbic, B. K., & Chassignet, E. P. (2023). *MOM6 M_2 tides with porous barriers* [dataset]. Zenodo. Retrieved from https://doi.org/10.5281/zenodo.8166251 doi: 10.5281/zenodo.8166251

Wunsch, C. (1972). Bermuda sea level in relation to tides, weather, and baroclinic fluctuations. *Reviews of Geophysics*, *10*(1), 1–49.